npj Computational Materials

www.nature.com/npjcompumats

ARTICLE OPEN

Check for updates

Multifunctional antiperovskites driven by strong magnetostructural coupling

Harish K. Singh[1]✉, Ilias Samathrakis[1], Nuno M. Fortunato[1], Jan Zemen[2,3], Chen Shen[1], Oliver Gutfleisch[1,4] and Hongbin Zhang[1]✉

Based on density functional theory calculations, we elucidated the origin of multifunctional properties for cubic antiperovskites with noncollinear magnetic ground states, which can be attributed to strong isotropic and anisotropic magnetostructural coupling. Of 54 stable magnetic antiperovskites M_3XZ (M = Cr, Mn, Fe, Co, and Ni; X = selected elements from Li to Bi except for noble gases and 4f rare-earth metals; and Z = C and N), 14 are found to exhibit the Γ_{4g}/Γ_{5g} (i.e., characterized by irreducible representations) antiferromagnetic magnetic configurations driven by frustrated exchange coupling and strong magnetocrystalline anisotropy. Using the magnetic deformation as an effective proxy, the isotropic magnetostructural coupling is characterized, and it is observed that the paramagnetic state is critical to understand the experimentally observed negative thermal expansion and to predict the magnetocaloric performance. Moreover, the piezomagnetic and piezospintronic effects induced by biaxial strain are investigated. It is revealed that there is not a strong correlation between the induced magnetization and anomalous Hall conductivities by the imposed strain. Interestingly, the anomalous Hall/Nernst conductivities can be significantly tailored by the applied strain due to the fine-tuning of the Weyl points energies, leading to promising spintronic applications.

npj Computational Materials (2021)7:98 ; https://doi.org/10.1038/s41524-021-00566-w

INTRODUCTION

Smart materials like multiferroic materials with enhanced coupling between different degrees of freedom (e.g., mechanical, electronic, and magnetic) are promising for engineering devices for future applications such as sensors, transducers, memories, and spintronics[1–3]. Cubic antiperovskite (APV) compounds host the two most appealing aspects of multiferroics, e.g., magnetoelectric coupling and piezomagnetic effect (PME)[3,4]. In APV materials, the strong magnetoelectric coupling is achieved by combining piezoelectric and piezomagnetic heterostructure composites[5–7]. A significant PME is reported for Mn-based nitrides like Mn_3SnN, making such compounds a suitable component for fabricating magnetoelectric composite[8,9]. The PME in APVs can be attributed to the strong magnetostructural coupling, which manifests itself also as giant negative thermal expansion (NTE)[10–12] and magnetocaloric/barocaloric effect[9,13–17]. From the materials perspective, many Mn-based APV carbides go through a first-order magnetic phase transition and possess a large magnetocaloric effect[14,18]. For instance, Mn_3GaC exhibits a huge magnetic entropy change (ΔS_M) of 15 J/kgK under an applied magnetic field of 2T[16]. The strong magnetostructural coupling in APVs is driven by the cubic-to-cubic first-order transition wherein a change in the crystal volume brings about a change in the frustrated magnetic states. Last but not least, APVs have been investigated recently due to the presence of a treasury of multifunctionality such as superconductivity[19], thermoelectric[20], magnetostriction[21].

Particularly, from the topological transport properties point of view, the existence of finite anomalous Hall conductivity (AHC) in noncollinear antiferromagnets has attracted noticeable attention due to possible applications in AFM spintronics for information storage and data processing[22–25]. The spin-dependent transport phenomena can provide spin-polarized charge current and large pure spin current, which could be achieved premised on two fundamental properties, i.e., AHC and spin Hall conductivity. The kagome lattice turns out to be an elementary model to host giant AHC[26–28]. Recently, Mn-based APV nitrides have been proposed to exhibit large AHC in frustrated AFM kagome lattice[29–32]. It is observed that Mn_3GaN exhibits vanishing and non-vanishing AHC for two different magnetic ordering Γ_{5g} and Γ_{4g}, respectively[29,30]. In this regard, for magnetic materials with noncollinear AFM ground states, the non-vanishing AHC is only feasible with specific magnetic space group symmetry, i.e., the AHC tensor depends on the magnetic group symmetry[33]. For instance, Mn_3X (X = Ga, Ge, and Sn) and Mn_3Z (Z = Ir, Pt, and Rh) have been reported to have a different form of AHC tensor as a result of different magnetic ordering[22,34–36]. A possible phase transition ($\Gamma_{5g} \leftrightarrow \Gamma_{4g}$) attained by strain or chemical modification could make these materials suitable for AFM spintronic applications. The spin-polarized current could also be generated by temperature gradient instead of the applied electric fields, resulting in anomalous Nernst conductivity (ANC), also termed as spin caloritronics[37,38]. A large ANC in noncollinear AFMs could be useful for establishing spin caloritronics devices that exhibit useful prospects in energy conversion and information processing. Noticeably, a large ANC of 1.80 $AK^{-1}m^{-1}$ has been reported for APV Mn_3NiN at 200 K[39], which is slightly less than half of the highest reported ANC of 4.0 $AK^{-1}m^{-1}$ in Co_2MnGa[40,41]. Enhancing the AHC and ANC by applying strain could be crucial for realizing AFM spintronic devices.

In this work, we carried out a systematic analysis of 54 cubic APV systems ($Pm\bar{3}m$) with chemical formula M_3XZ (see Supplementary Fig. 1) to determine their magnetic ground states, tunability via biaxial strain, and the resulting spintronic properties (Fig. 1). The selected 54 cubic APVs are stable, i.e., fulfilling all three stability criteria such as thermodynamical, mechanical, and dynamical stabilities, which were recently evaluated in our

[1]Institute of Materials Science, Technische Universität Darmstadt, Darmstadt, Germany. [2]Faculty of Electrical Engineering, Czech Technical University, Prague, Czech Republic. [3]Department of Physics, Blackett Laboratory, Imperial College London, London, UK. [4]Materials Recycling and Resource Strategies, Fraunhofer IWKS, Hanau, Germany. ✉email: harish@tmm.tu-darmstadt.de; hzhang@tmm.tu-darmstadt.de

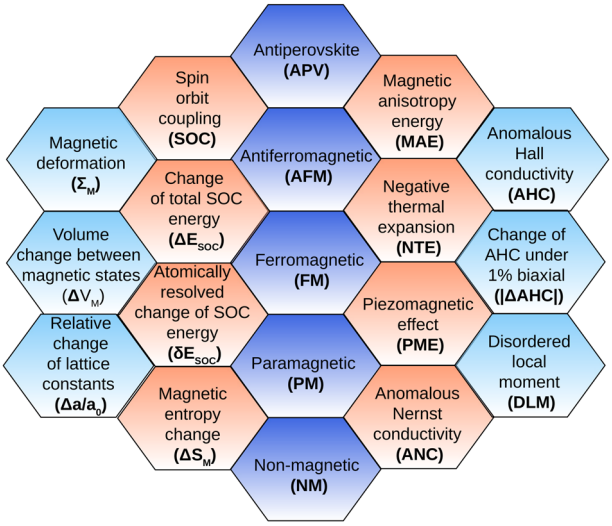

Fig. 1 Abbreviations. The list of abbreviations used in the manuscript.

high-throughput screening[42]. Explicit calculations were performed to obtain the energies of eight phases, i.e., Γ_{4g}, Γ_{5g}, non-magnetic (NM), ferromagnetic (FM), collinear AFM-1 (cAFM-1), collinear AFM-2 (cAFM-2), collinear AFM-3 (cAFM-3), and M-1 configurations. Moreover, the magnetic anisotropy energy (MAE) defined as the energy difference between Γ_{5g} and Γ_{4g} is examined to understand the origin of the noncollinear magnetic states with the help of spin-orbit coupling (SOC) energy. Moreover, a detailed analysis of the lattice constant variation with respect to the magnetic states reveals that the paramagnetic (PM) state is critical in the magnetic phase transition, enabling us to predict potential NTE and magnetocaloric materials. Last but not least, the PME was studied by introducing biaxial strains (compressive and tensile), which causes possible phase transitions between $\Gamma_{5g} \leftrightarrow \Gamma_{4g}$, and leads to a significant modification in the AHC and ANC, dubbed as a piezospintronic effect[30,43]. In-depth analysis on symmetry analysis and electronic structure suggests that the piezospintronic effect is originated from the existence of Weyl nodes whose position can be tailored by strain, resulting in promising applications for future spintronic devices.

RESULTS

Validation and prediction of magnetic ground state

As the magnetic transition metal atoms are located at the face centers of the cubic cell for magnetic APVs, it leads to a frustrated kagome lattice in the (111)-plane. Correspondingly, noncollinear magnetic structures are expected when the interatomic exchange interaction is AFM for the nearest neighbors. As shown in Fig. 2, Γ_{4g} and Γ_{5g} are the two most common magnetic configurations reported for APVs, resulting in 120° magnetic angle configurations within the (111)-plane between three magnetic moments. The Γ_{4g} state can be obtained from Γ_{5g} by simultaneously rotating the moments of three metal atoms within the (111)-plane by 90°. The APVs with the noncollinear magnetic ground state are listed in Table 1, in comparison to the available experimentally measured results. Interestingly, all the APVs with noncollinear magnetic ground states are nitrides including Cr and Mn, while all carbides end up with the FM and cAFM-2 ground state except Mn_3SnC, which exhibits the Γ_{5g} state (see Supplementary Table 1).

Mn_3GaC[44] and $Mn_3Ga_{0.95}N_{0.94}$[15] are reported to adopt collinear AFM and M-1 magnetic configurations, respectively. Thus, we considered additionally cAFM-1, cAFM-2, cAFM-3, and M-1 configurations (see Fig. 2e–h). It is confirmed that Mn_3GaC exhibit the cAFM-2 magnetic ground state, the same as Mn_3AlC and Mn_3InC. This is in contrast to the previous experimental reports on both Mn_3AlC[45] and Mn_3InC[46] with a FM configuration. Moreover, Cr_3SnN and Mn_3SnN exhibit the cAFM-3 magnetic ground state, where it is demonstrated that Mn_3SnN shows four different magnetic and crystallographic phases (see Supplementary Note 1)[47,48]. Such discrepancies might be attributed to the temperature effect, indicating a strong interplay between magnetism and crystal structures at finite temperatures that deserves further detailed investigations. Interestingly, none of the APV is stabilized in the M-1 phase (see Supplementary Table 1). It is noted that there are also other magnetic configurations such as ferrimagnetic and canted states for Mn_3XC (X = Sn and Zn), which will be saved for future investigations.

The magnetic ground states of noncollinear APVs are in good agreement with the experimental measurements. For instance, both Mn_3GaN[13] and Mn_3ZnN[47,49] have the Γ_{5g} magnetic ground state, which are consistent with our density functional theory (DFT) calculations. Interestingly, many Mn-based APVs exhibit a mixed $\Gamma_{4g} + \Gamma_{5g}$ magnetic ordering, with a possible meta-magnetic transition to the other magnetic phases[47]. For instance, Mn_3AgN is characterized by two distinct magnetic phase transitions. A mixed $\Gamma_{4g} + \Gamma_{5g}$ phase exists below 55 K, whereas pure Γ_{5g} state persists at intermediate temperature range (55 K < T < 290 K), and lastly, it undergoes the magnetic transition to PM state at 290 K[47]. Likewise, Mn_3NiN displays such mixed magnetic phases[47].

The mixed magnetic ordering can be attributed to the MAE between the Γ_{5g} and Γ_{4g} states, which can be expressed as:

$$MAE = E_{\Gamma_{5g}} - E_{\Gamma_{4g}}, \quad (1)$$

where E indicates the total energy of the corresponding magnetic configuration. For Mn_3AgN and Mn_3 NiN with experimentally observed mixed magnetic states, the corresponding MAE is 0.063 and 0.144 meV, respectively. Nevertheless, it is still unclear why Mn_3AgN is stabilized in the Γ_{5g} state between 55 and 290 K. We suspect that those compounds with MAE greater than 0.2 meV between Γ_{4g} and Γ_{5g} should have pure noncollinear magnetic states. In our study, the Mn-based APVs Mn_3XN with X = Ag, Co, Ir, Ni, Pd, and Rh exhibit Γ_{4g} while those with X = Au, Ga, Hg, In, Pt, and Zn display the Γ_{5g} as the magnetic ground state (see Table 1 and Supplementary Table 1). This is consistent with the recent DFT calculations for Mn_3XN (X = Ni, Zn, Ga, and Pt)[50], except for Mn_3XN (X = In, Pd, and Ir). In ref. [50], Mn_3InN exhibit Γ_{4g} state while Mn_3XN (X = Ir and Pd) display Γ_{5g} state. The MAE for Mn_3InN calculated by Huyen et al. is 74.6 meV, which is much larger than our MAE (–1.84 meV). As detailed below, a large MAE could be expected for the compound with strong SOC; thus, it is questionable for Mn_3InN with such a large MAE of 74.6 meV[50]. To clarify the discrepancy, we performed calculations of the MAE using the Quantum Espresso (QE) code[51] with the same parameters consider in Huyen et al. study. The QE and VASP calculations provide the same magnetic ground state and MAE for Mn_3XN (X = Ir and Pt) systems, which is in contradiction to the Huyen study performed using QE[50].

Lastly, based on our high-throughput calculations[42], two unreported Cr-based APVs are stable, our calculations reveal that Cr_3IrN and Cr_3PtN have Γ_{4g} as the lowest energy magnetic configuration (see Table 1 and Supplementary Table 1). While among APV nitrides, Mn_3AuN and Mn_3HgN are the other two unreported noncollinear systems with Γ_{5g} magnetic ground state. To the best of our knowledge, there is no experimental neutron diffraction measurement available till now for such APVs, making them interesting for future studies. To shed more light on the origin of MAE, we performed detailed calculations of the SOC energy in order to obtain atomically resolved contributions to the MAE. Like MAE, the change in the total SOC energy (ΔE_{SOC}) of M_3XN can be defined as the difference between the SOC energy

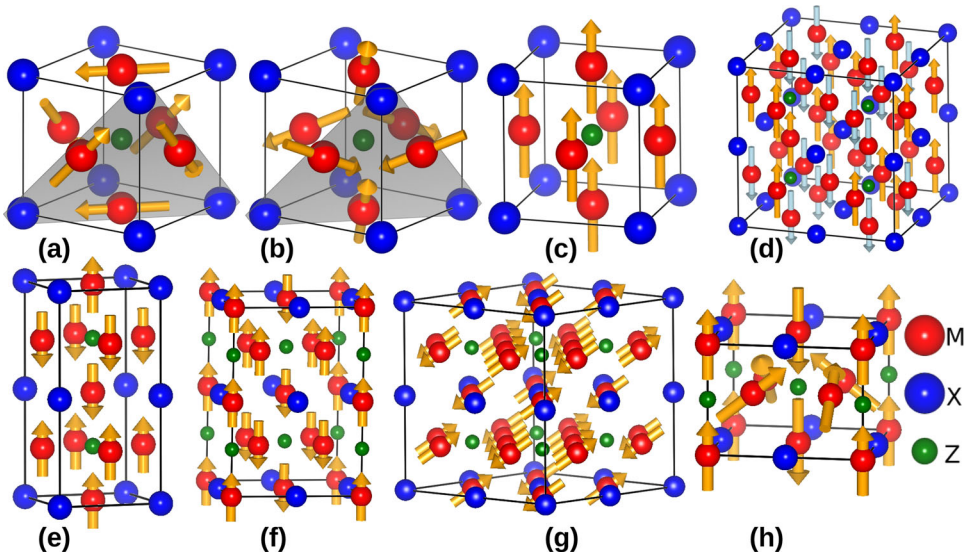

Fig. 2 Magnetic configurations. Possible magnetic structures of antiperovskites: **a** Γ_{5g}, **b** Γ_{4g}, **c** FM, **d** PM, **e** cAFM-1, **f** cAFM-2, **g** cAFM-3, and **h** M-1. The spin chirality for Γ_{4g} and Γ_{5g} is assumed to be +1.

Table 1. Compilation of the APVs (M_3XZ) with noncollinear magnetic ground state.

M_3XZ	magGS	$^{M}(\delta E_{SOC})$	$^{X}(\delta E_{SOC})$	ΔE_{SOC}	MAE	Refs.
Cr_3IrN	Γ_{4g}	−0.367	4.532	4.164	2.187	
Cr_3PtN	Γ_{4g}	−0.936	5.639	4.703	2.868	
Mn_3AgN	Γ_{4g}	0.3987	−0.2486	0.151	0.063	Γ_{4g}+Γ_{5g} ref. [47]
Mn_3AuN	Γ_{5g}	1.205	−4.353	−3.148	−1.671	
Mn_3CoN	Γ_{4g}	0.005	1.716	1.721	1.218	AFM ref. [11]
Mn_3GaN	Γ_{5g}	−1.111	1.10	−1.110	−0.291	Γ_{5g} ref. [47,71]
Mn_3HgN	Γ_{5g}	−0.746	−3.691	−4.438	−1.551	
Mn_3InN	Γ_{5g}	−0.734	−0.224	−0.958	−1.849	
Mn_3IrN	Γ_{4g}	0.599	19.705	20.305	10.548	
Mn_3NiN	Γ_{4g}	1.216	−0.87	0.346	0.144	Γ_{4g}+Γ_{5g} ref. [47]
Mn_3PdN	Γ_{4g}	1.292	−1.115	0.176	0.357	AFM ref. [11]
Mn_3PtN	Γ_{5g}	3.872	−13.877	−10.005	−4.969	
Mn_3RhN	Γ_{4g}	−0.021	3.482	3.460	1.702	
Mn_3ZnN	Γ_{5g}	−0.756	−0.105	−0.861	−1.452	Γ_{5g} refs. [47,49]

All the units are in meV. For each compound, the calculated magnetic ground state (magGS) is listed and the change in the atomically resolved SOC energy (δE_{SOC}) between Γ_{5g} and Γ_{4g} state is enumerated for M and X atoms. The calculated MAE and ΔE_{SOC} are summarized as given by Eqs (1) and (2), respectively. The last column lists the available experimental magnetic ground state.

(E_{SOC}) of the Γ_{5g} and Γ_{4g} magnetic states[52].

$$\Delta E_{SOC} = E_{SOC}(\Gamma_{5g}) - E_{SOC}(\Gamma_{4g}), \quad (2)$$

In the same way, the atomically resolved change of SOC energy (δE_{SOC}) can also be defined for each atomic species, as shown in Table 1 and Supplementary Table 3. The positive (negative) values of MAE and ΔE_{SOC} indicate the Γ_{4g} (Γ_{5g}) magnetic ground state. On the one hand, it is found that the sign of MAE is the same as that of ΔE_{SOC} (see Table 1). That is, both the ΔE_{SOC} and MAE are equally valid to characterize the magnetic ground states, with a linear scaling behavior observed (see Supplementary Fig. 2). For example, Cr_3PtN has Γ_{4g} magnetic ground state with an MAE of 2.868 meV and ΔE_{SOC} of 4.70 meV. The atomic resolved δE_{SOC} of Pt and Cr are 5.639 and −0.938 meV. Evidently, the δE_{SOC} of Pt is larger than Cr δE_{SOC} originating in the strong SOC of Pt. As a result, the δE_{SOC} of Pt is a determining factor for the MAE and ΔE_{SOC} sign. On the other hand, for most APVs, the contribution of the X elements to MAE is more significant than that of the magnetic elements M, as indicated by the atomic resolved δE_{SOC} (see Table 1). Taking the Mn_3XN with X = Co, Rh, and Ir as examples, the MAE are 1.22, 1.70, and 10.55 meV, corresponding to the dominant δE_{SOC} of X as 1.72, 3.46, and 20.31 meV, respectively. It is noted that δE_{SOC} of Mn is smaller than 3% of ΔE_{SOC} for such compounds. This can be attributed to the enhanced strength of atomic SOC of the X elements, e.g., the strength of atomic SOC for Co, Rh, and Ir atoms is about 0.065, 0.152, and 0.452 eV, respectively[53]. Therefore, the enhanced atomic SOC strength of the X elements is favorable for the strong MAE of the APV compounds.

NTE and barocaloric

Turning now to the magnetostructural coupling, which can be best represented for APVs by the NTE, magnetocaloric, and PME. NTE materials exhibit contraction in the lattice parameters with respect to temperature in contrast to most materials.[49] To study NTE of APVs, we evaluated the relative change in the lattice constants $\Delta a/a_0$ on the transition from the noncollinear magnetic ground state to PM state (where a_0 is the lattice constant of Γ_{4g} or Γ_{5g} noncollinear state and Δa is lattice constant difference between PM and Γ_{4g} or Γ_{5g} state) and compared with the $\Delta a/a_0$ values obtained from the experimental measurement at their transition temperature (see Fig. 3a)[11,12,49]. The average of the evaluated $\Delta a/a_0$ is in good agreement with the experimental observation except for Mn_3GaN (see 3a). Together with the mismatch for the other cases, we suspect it may be due to the finite temperature effect, as our DFT calculations are done at zero Kelvin.

Importantly, it is found that the PM state is critical and cannot be approximated as the NM state, e.g., the $\Delta a/a_0$ between the noncollinear and NM states is about five times as large as the experimental value (see Fig. 3a). An ameliorated estimation could be achieved by defining the PM phase as a collinear AFM arrangement generated by using the disordered local moment (DLM) theory[54]. The $\Delta a/a_0$ of Cr_3IrN and Cr_3PtN on the transition

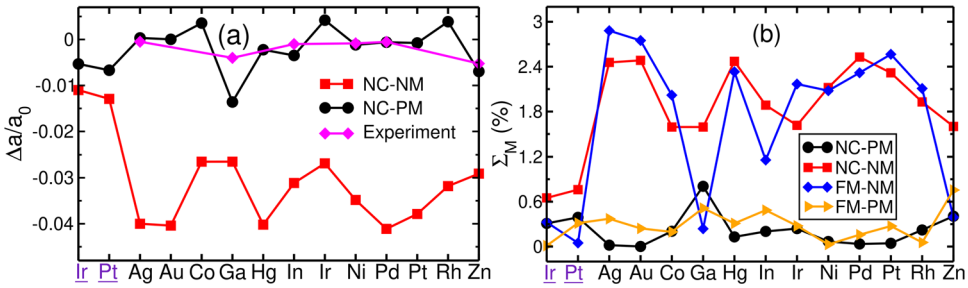

Fig. 3 Negative thermal expansion and barocaloric. a The relative change in the lattice constant ($\Delta a/a_0$) and **b** the magnetic deformation Σ_M for the $Cr_3\underline{X}$ N and Mn_3XN antiperovskites ($\underline{X}$ and X are the elements present on the *x*-axis in violet and black, respectively). The lattice constants of noncollinear, FM, PM, and NM states are used to determine $\Delta a/a_0$ and Σ_M.

from Γ_{4g} magnetic ground state to PM are –0.0053 and –0.0067, respectively. That is, Cr-based APVs undergo the lattice contraction with $\Delta a/a_0$ comparable to the reported NTE in Mn-based APV materials such as Mn_3GaN and Mn_3ZnN (see Fig. 3a). Furthermore, the equilibrium lattice constants decrease and increase for the Mn_3XN (X = Ga, Hg, In, Ni, Pd, Pt, and Zn) and Mn_3XN APVs (X = Au, Co, Ir, and Rh) on the transition from a noncollinear magnetic ground state to PM state, respectively (see Fig. 3a).

Recently, Bocarsly et al. proposed a magnetic deformation proxy Σ_M to predict the magnetocaloric materials as the theoretical evaluation of (ΔS_M) is very challenging[55]. This proxy measures the volume deformation of the NM and magnetic structure, which correlates well with the experimentally measured ΔS_M values. In their study, they screened 167 FM materials, including 7 APVs. For the APVs, it is noted that Σ_M scales linearly with the percentage volume difference ΔV_M between the FM and NM unit cell (see Supplementary Fig. 3). Inspired by their work, we evaluated Σ_M for the APVs with FM and noncollinear magnetic ground state in order to estimate the potential magnetocaloric effect. For FM APVs, it is found that the Σ_M is most significant for the Fe-based APVs within the 1.2–1.7% range (see Supplementary Table 5). For example, the Σ_M of Fe_3RhN, Fe_3PtN, and Fe_3NiN are 1.67%, 1.59%, and 1.54%, respectively, whereas Co-, Mn-, and Ni-based APVs have $\Sigma_M < 1.0\%$ except for Mn_3ZnC (1.33%) (see Supplementary Table 5). Thus, we expect a significant magnetocaloric effect in Fe_3RhN, Fe_3PtN, and Fe_3NiN, based on the argument that the Σ_M approximate to 1.5% could exhibit a considerable magnetocaloric effect[55].

As to the noncollinear APVs, we evaluated the Σ_M by considering four ΔV_M combinations, namely, the noncollinear magnetic ground state with PM and NM states (NC-PM and NC-NM), the FM with PM and NM states (FM-PM and FM-NM) (see Fig. 3b and Supplementary Table 6). It is observed that the Σ_M value is small by using the ΔV_M of the NC-PM and FM-PM states, in comparison to the other two combinations (see Fig. 3b). Nevertheless, a small value of Σ_M does not mean a low ΔS_M[55]. For instance, the experimentally measured ΔS_M of Mn_3GaN is very significant (22.3 $Jkg^{-1}K^{-1}$), and it also exhibits giant barocaloric effect[13]. Overall, the Σ_M of Mn_3GaN should be largest among all the APVs. The calculated Σ_M of Mn_3GaN is largest 0.805% for the Γ_{5g} and PM state combination, which verifies the experimental observation, whereas the Σ_M of Mn_3GaN for the other three combinations is not the largest among the APVs (see Fig. 3b). Therefore, it can be concluded for the noncollinear systems that the approach of Bocarsly et al. proxy does not provide reasonable Σ_M obtained from the ΔV_M combination of NC-NM, FM-NM, and FM-PM states. The implicit correlation of ΔS_M with Σ_M indicates the strong magnetostructural coupling in APVs with significant ΔV_M (NC-PM). This conduces to the prediction of possible NTE and magnetocaloric materials with sizable Σ_M by virtue of significant ΔV_M (see Supplementary Table 6). For example, the Cr_3XN APVs (X = Ir and Pt) with appreciable Σ_M could exhibit potential applications as NTE and magnetocaloric materials.

Piezomagnetism

PME provides another effective characterization of the magnetostructural coupling[6], which manifests itself as the response of magnetization to strain. The origin of PME is explained based on symmetry together with an illustration of the magnetic spin directions (see Supplementary Fig. 4 and Supplementary Note 2). For APVs with noncollinear magnetic ground states, the total bulk magnetization is vanishing, but a net magnetization can be induced under finite compressive/tensile strain, as reported for Mn-based APVs[6,8]. Our calculations confirm their results on the Mn-based APVs except for the Mn_3CoN and Mn_3RhN (see Supplementary Fig. 5), where the resulting net magnetization from our (Zemen et al.)[8] calculations are 0.646 (0.305) and 0.214 (−0.143) μ_B/f.u., respectively. Interestingly, for Mn_3CoN, a net magnetic moment of 0.362 μ_B/f.u. is induced at Co atoms under 1% tensile strain, whereas the local magnetic moment of Co is zero in the cubic unstrained state. The magnetic moment direction of Co is aligned in (111) plane similar to Mn atom direction in the Γ_{4g} state. As a result, Mn_3CoN could be an interesting material for elastocaloric and magneto-elastic applications. Surprisingly, the PME effect is asymmetric with respect to the applied compressive and tensile strains (see Supplementary Figs. 6 and 7). Most APVs exhibit more significant PME with tensile strain except Cr_3PtN (see Supplementary Fig. 6), e.g., the net magnetization for Cr_3PtN at 1% compressive strain is as large as 0.21 μ_B/f.u. in comparison to 0.15 μ_B/f.u. at 1.0% tensile strain.

The magnitude of the magnetoelectric effect is minimal in the intrinsic bulk AFM materials, such as Cr_2O_3[56]. The two-phase heterostructure materials consolidate the magnetoelectric effect. A recent study corroborates APV as a potential material for magnetoelectric composite[6,57]. The piezoelectric perovskite could be one suitable substrate for such composite heterostructure as they also have comparable lattice parameters with APVs[5,58]. The heterostructure amalgamate the piezoelectric and piezomagnetic properties, which are coupled by an interfacial strain. Based on our PME analysis, we propose Cr- and Mn-based noncollinear systems with significant PME as potentials candidates for magnetoelectric composite.

Interestingly, the biaxial strain can induce phase transition between different magnetic configurations, i.e., Γ_{4g} and Γ_{5g}, which can further lead to a significant change in the transport properties as discussed below. It is found that a few APV materials undergo a magnetic phase transition due to the imposed biaxial strain (see Supplementary Tables 4 and 7). For instance, cubic Mn_3AuN has Γ_{5g} as the magnetic ground state, which preserves under tensile strain. However, a transition into a distorted Γ_{4g} state is obtained by applying a compressive strain of 0.5 and 1.0% (see Supplementary Table 4). Such transitions can be attributed to significant changes in the MAE and with respect to the biaxial strain (see Supplementary Table 4), but there is no consistent MAE trend as the absolute value of MAE is mostly determined by the atomic SOC strengths.

Anomalous Hall conductivity (unstrained)

It is well known that FM compounds commonly exhibit AHC due to the presence of a net magnetization[59], where the broken time-reversal symmetry ($\mathcal{T}$) and SOC are two essential prerequisites. Noncollinear AFMs also display non-zero AHC, as observed in Mn_3X (X = Ir, Ge, and Sn)[22,34]. As a linear response property, the occurrence of AHC can be elucidated based on the symmetry analysis. For cubic APVs, the magnetic space group of Γ_{5g} and Γ_{4g} are $R\bar{3}m$ (166.97) and $R\bar{3}m'$ (166.101), respectively. For Γ_{5g}, the local magnetic moment spin directions of M atoms are invariant under the mirror symmetry transformation $M_{(0\bar{1}1)}$, $M_{(10\bar{1})}$, and $M_{(\bar{1}10)}$, leading to vanishing AHC (see Supplementary Table 8)[29,30], whereas in the Γ_{4g} state, the above-mentioned mirror symmetries are broken, but the product of mirror (M) and time-reversal symmetry $\mathcal{T}$ retain the Γ_{4g} configuration. This results in finite AHCs with all three off-diagonal components non-zero but of the same amplitude (see Supplementary Table 8)[29].

Explicit calculations confirm the above symmetry arguments. For instance, the AHC is zero for Mn_3XN (X = Au, Hg, In, Pt, and Zn) with the Γ_{5g} ground state (see Supplementary Figs. 8b and 9), whereas the significant AHC is observed for the APVs with the Γ_{4g} ground state, such as the AHC of Cr_3IrN and Cr_3PtN are 414.6 and 278.6 S/cm, respectively. The AHC of APVs is summarized in the Supplementary information (see Supplementary Figs. 8–10 and 16). In comparison to the previous studies on an individual or a few compounds[29,32], our results are in good agreement (see Supplementary Table 9). For instance, the AHC of Mn_3SnN from our and calculations by Gurung et al. are 106.5 and 133 S/cm[29], respectively, whereas the value (−73.9 S/cm) obtained by Huyen et al.[50] is of opposite sign in addition to the difference in the absolute values. In this regard, for Mn_3NiN, the sign of experimentally observed AHC is confirmed by our DFT calculations[31], consistent with that obtained by Zhou et al[32,39]. This might be due to opposite magnetization direction while maintaining the noncollinear configurations or chirality of noncollinear spin configurations specified in the calculations, subject to further investigations. Moreover, it is observed that the absolute values of AHC for the same compound in the same magnetic ground state are scattered as well (see Supplementary Table 9). We suspect that this is due to the different lattice constants and numerical parameters used in different calculations. For instance, Zhou et al. performed calculations using the experimental lattice constants on Mn_3NiN and other APV compounds, which are on average about 1.0–1.3% smaller than the fully relaxed lattice constants in this work.

Strain-induced AHC (piezospintronics)

As discussed above, all cubic APVs with noncollinear magnetic ground states display significant PMEs where a net magnetization can be induced by applying biaxial strain; an interesting question is whether the AHC can be tailored as well. From the symmetry point of view, for the Γ_{5g} state, the magnetic space group changes from $R\bar{3}m$ (166.97) to $C2/m$ (12.58) with biaxial strain, resulting in finite σ_x and σ_y with the same amplitude but opposite sign, while the σ_z component remains zero[30]. This is confirmed by our calculations on those compounds with the Γ_{5g} ground state. For instance, the AHC induced by 1% biaxial strain is as large as −71.2 S/cm for Mn_3PtN (see Supplementary Fig. 8b), comparable to that in Mn_3HgN (see Supplementary Fig. 9). The Mn_3InN and Mn_3ZnN have quite low AHC due to weak SOC strength (see Supplementary Fig. 9).

Similarly, the AHC of APVs in the Γ_{4g} state can also be tailored by the biaxial strain. In this case, the magnetic space group is reduced from $R\bar{3}m'$ (166.101) to $C2'/m'$ (12.62), the resulting σ_x and σ_y components are the same while the σ_z component possesses a distinct value (see Supplementary Fig. 8a and Supplementary Table 8). Explicit evaluations of the AHC for APVs in distorted Γ_{4g} states verify the symmetry arguments, where the σ_x and σ_y components behave the same with respect to strain (see Supplementary Fig. 8a). Interestingly, it is observed that more significant changes occur in AHC for the Γ_{4g} compounds than the Γ_{5g} cases. For instance, the σ_z component of AHC in Cr_3IrN attains the largest AHC of 693.1 S/cm at 1% tensile strain, with an increase of 278 S/cm compared to the value in the cubic geometry (see Supplementary Fig. 8a). Moreover, the moderate strain can even lead to a sign change of the AHC, as observed on the σ_z component of Mn_3AgN and Mn_3CoN with 0.5% compressive and 1% tensile strain, respectively (see Supplementary Fig. 10).

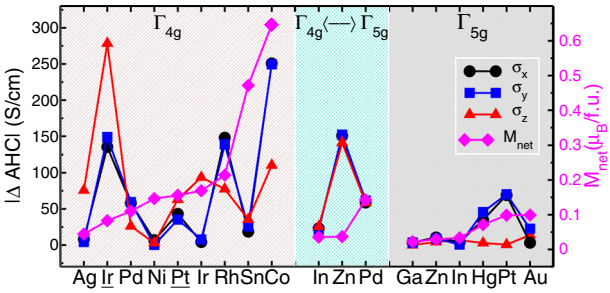

Fig. 4 Piezospintronic. The piezospintronic effect is illustrated by the change in AHC (|ΔAHC|) at 1% tensile strain and cubic phase. The |ΔAHC| and net magnetization is shown for the $Cr_3\underline{X}$ N and Mn_3XN antiperovskites ($\underline{X}$ and X are the elements present on the x-axis, respectively). The left, middle, and right panels correspond to the Γ_{4g}, phase transition between Γ_{4g} and Γ_{5g}, and Γ_{5g} state, respectively.

One interesting question is whether the piezospintronic effect (i.e., the variation of AHC induced by biaxial strain) correlates with the PME, as summarized in Fig. 4 for the variation of such quantities comparing the cases with 1% tensile strain and cubic geometries. Obviously, |ΔAHC| cannot be directly inferred from the induced net magnetization, particularly exemplified by the APVs in the Γ_{4g} magnetic ground state. For example, the |ΔAHC| and net magnetization of Cr_3IrN are 278.5 S/cm (σ_z component) and 0.082 μ_B/f.u., respectively, while for Mn_3SnN, the |ΔAHC| and net magnetization are 35.5 S/cm (σ_z component) and 0.47 μ_B/f.u., respectively. Moreover, for Mn_3CoN, the net magnetization and |ΔAHC| of σ_x are 250.7 S/cm and 0.646 μ_B/f.u. It signifies that the |ΔAHC| could be large for the small net magnetization and vice versa (see Fig. 4). Interestingly, the |ΔAHC| and net magnetization are smaller for those compounds in the Γ_{5g} magnetic state, in comparison to those of such materials with the Γ_{4g} magnetic state, e.g., the |ΔAHC| and net magnetization of Mn_3ZnN are 9.17 S/cm and 0.029 μ_B/f.u., respectively.

Particularly, the APVs undergoing a phase transition between Γ_{4g} and Γ_{5g} states driven by the epitaxial strain exhibit strong piezospintronic effect while the magnitude of the PME is marginal. For instance, Mn_3ZnN has a Γ_{5g} magnetic ground state in the cubic phase with vanishing AHC. A phase transition into the Γ_{4g} state by 1% tensile strain results in a considerable |ΔAHC| of 152.2 S/cm for the σ_y component (see Fig. 4). On the other hand, the phase transition from the Γ_{4g} to Γ_{5g} states for Mn_3PdN leads to a |ΔAHC| as large as 58.6 S/cm (Fig. 4). Therefore, we suspect that those compounds with Γ_{4g} states are more promising to host a strong piezospintronic effect.

Anomalous Nernst effect

The intriguing behavior of AHC under biaxial strain can be attributed to the fine-tuning of the electronic structure. To further illustrate such sensitivity, we investigated the ANC, which shares the same symmetry as AHC but is proportional to the derivative of AHC with respect to energy following the Mott formula[60]. Taking

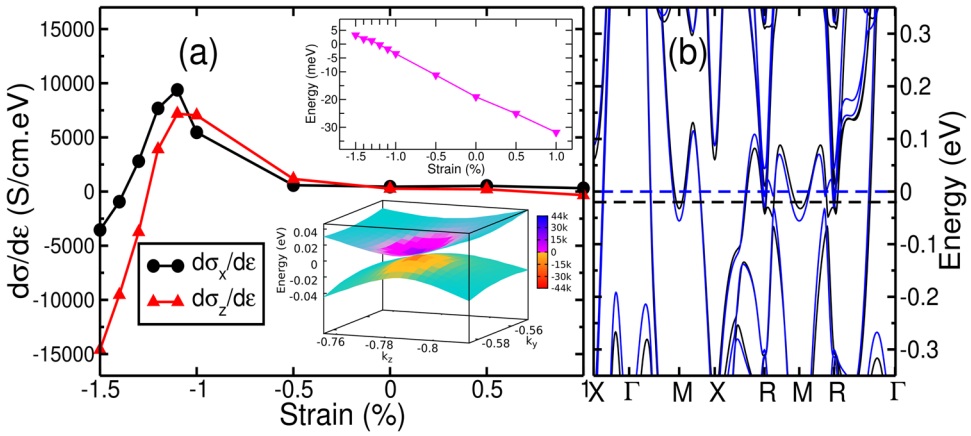

Fig. 5 Anomalous Nernst effect. a The calculated ANC of Mn_3PdN in the Γ_{4g} magnetic state. The Weyl points (0.43, −0.35, −0.49, and equivalent coordinates) shift across the Fermi level with strain (inset above) and the Berry curvature for the 1.4% compressive biaxial strain (inset below). **b** The band structure of Mn_3PdN for unstrained (black) and 1.4% compressive biaxial strained (blue). The presence of Weyl point near the Fermi energy is indicated by black (cubic) and blue dashed line (−1.4% biaxial strain).

Mn_3NiN as an example, the corresponding ANC is as large as 16,569 S/cm.eV. This is consistent with 1.80 $AK^{-1}m^{-1}$ at 200 K obtained by Zhou et al.[39], up to a factor of two but with alike dependence with respect to the energy around the Fermi energy (see Supplementary Fig. 15). The numerical discrepancy might be due to the different lattice constants used in the calculations, as discussed above. Such a large ANC of Mn_3NiN is comparable to the largest values observed experimentally in Co_2FeGe (3.16 $AK^{-1}m^{-1}$), Co_2MnGa (4.0 $AK^{-1}m^{-1}$), and Fe_3Ga (3.0 $AK^{-1}m^{-1}$)[40,41,61,62]. Interestingly, the strain also has a stronger influence on the ANC. For the tetragonally distorted Mn_3NiN in the Γ_{4g} state, the ANC becomes as large as 20,035 S/cm.eV at −0.5% compressive strain for the α_x and α_y components, i.e., enhanced by 21% compared to that of the cubic case. Last but not least, a sign change can be induced in the ANC by the biaxial strain. For instance, the ANC corresponding to the α_x and α_y components of Cr_3IrN changes to −3196.9 S/cm.eV at 1% compressive strain starting from 6823.4 S/cm.eV for the cubic case in the Γ_{4g} state. This is also observed for Mn_3AgN and Mn_3CoN (see Supplementary Fig. 11). The ANC of APV compounds as a function of biaxial strain is summarized in Supplementary Figs. 11–14.

To explicate the origin of the piezospintronic effects on both AHC and ANC, our detailed analysis of the electronic structure reveals that the tunability of AHC and ANC by strain can be attributed to the presence of Weyl points close to the Fermi energy. Taking Mn_3PdN as an example, as shown in Fig. 5a, the ANC can be tuned between 7037.3 S/cm.eV at 1% compressive strain to −14,599 S/cm.eV at 1.5% compressive strain, with a sign change at 1.3% strain. Such an ANC is comparable to that observed in Mn_3NiN, awaiting further experimental validation. The band structure shows no obvious changes due to the applied strain (see Fig. 5b). However, it is found that there are 12 Weyl points at (0.43, −0.35, and −0.49) and equivalent k-points with an energy of 20 meV below the Fermi energy in the cubic phase. Such Weyl points will be shifted across the Fermi energy upon applying compressive strain, e.g., reaches to −1.75 meV for −1.3% biaxial strain, and 1.87 meV above the Fermi energy for 1.4% strain (see above inset of Fig. 5a). The AHC is mostly enhanced when the Weyl points are located at the Fermi energy, due to the singular behavior of the Berry curvature at the Weyl nodes (see below inset of Fig. 5a). This is consistent with ref. [50] and our observation in Mn_3GaN[30,50]. For magnetic materials, the Weyl nodes with opposite chiralities (i.e., Berry curvatures with opposite sign) are located at the same energy, but the total contributions to the AHC can be significant, particularly if the Weyl nodes are within "several" or "a few" meV around the Fermi energy. Correspondingly, the sign of ANC, which is determined by the derivative of AHC can be tuned as the Weyl points are shifted across the Fermi level. We suspect such tunability of AHC and concomitant ANC by manipulating the Weyl points with the biaxial strain or other possible stimuli is promising for future applications, such as Fe_3Al with giant transversal thermoelectric effects[62].

DISCUSSION

We carried out a systematic analysis of 14 cubic APV M_3XZ compounds with noncollinear magnetic ground states, focusing on the magnetic properties driven by isotropic and anisotropic magnetostructural coupling. It is found that there exists a strong competition between different noncollinear magnetic configurations where a large MAE clearly defines the noncollinear magnetic ground state, while small MAE leads to the mixed Γ_{4g} and Γ_{5g} configurations. For such materials with mixed magnetic ions, the MAE cannot be understood based on the perturbation theory, whereas the SOC energy can be used to get a reliable atomic resolved contribution, which is mostly determined by the strength of atomic SOC. The magnetic ground state analysis resulted in the prediction of four unreported APVs with noncollinear ground state, especially Cr_3XN APVs (X = Ir and Pt) with the Γ_{4g} magnetic configuration. The isotropic magnetostructural coupling indicated by the magnetic deformation $\Delta a/a_0$ can be considered as an effective descriptor for the magnetocaloric effect. However, we observed that the magnetic deformation is better measured comparing the PM and magnetically ordered states, resulting in better agreement with the experimental NTE results, rather than comparing the NM and ordered state. Therefore, we suggest that the recently proposed proxy for predicting magnetocaloric effects based on the magnetic deformation could be improved by using quasi-random approximation of the PM state. More interestingly, biaxial strain not only causes a significant PME in such materials but also leads to a strong influence on MAE, AHC, and ANC after considering SOC. Based on detailed symmetry analysis, we performed an explicit evaluation of the AHC and found that those compounds with the Γ_{4g} magnetic ground state have large AHC, which is susceptible to the epitaxial strain. Nevertheless, there is no strong correlation between the net magnetization and induced AHC when finite strain is applied. Detailed analysis reveals that the sensitivity of AHC and derived ANC with respect to strain can be attributed to the fine-tuning of energies for the Weyl nodes, opening up further possibilities for engineering spintronic devices in the future.

METHODS

Density functional theory calculation

Our DFT calculations are performed using the projector augmented wave method as effectuated in the VASP package[63]. The exchange-correlation functional is approximated using the generalized gradient approximation as parameterized by Perdew–Burke–Ernzerhof[64]. We used an energy cutoff of 500 eV for the plane-wave basis set, and a uniform k-points grid of $13 \times 13 \times 13$ within the Monkhorst-pack scheme for the Brillouin zone integrations. The Methfessel–Paxton scheme is used to determine the partial occupancies of orbitals with a smearing width of 0.06 eV. The SOC is considered in all the calculations. In order to verify the magnetic ground state of various compounds, the more accurate total energy calculations are performed using a higher energy cutoff of 600 eV and a dense k-mesh of $25 \times 25 \times 25$ (see Supplementary Note 3).

The magnetic ground states are obtained by comparing the total energies (see Supplementary Table 1) of eight magnetic configurations, i.e., Γ_{4g}, Γ_{5g}, NM, FM, cAFM-1, cAFM-2, cAFM-3, and M-1 states (see Fig. 2), where the lattice constants are fully optimized for Γ_{4g}, Γ_{5g}, FM, PM, and NM state (see Supplementary Table 2). To verify the effects of the Coulomb interaction, we performed a series of DFT+U (U = 2–10 eV for the Mn-3*d* orbitals) calculations on Mn_3GaN. It is observed that the Γ_{5g} magnetic ground state does not change with respect to the applied U values (see Supplementary Table 10). Therefore, we suspect that the Coulomb interaction is likely to have a marginal influence on the magnetic ground state of such a class of compounds. Moreover, to investigate the piezomagnetic and piezospintronic effects, biaxial in-plane strain is applied, which reduces the crystalline symmetry from cubic to tetragonal. The optimal lattice constants along c-direction are evaluated by the polynomial fitting of the energies from a series of calculations.

Modeling of paramagnetic state

The PM state is modeled based on the DLM picture (see Fig. 2d), where a special quasi-random structure modeled using a $2 \times 2 \times 2$ supercell by imposing zero total magnetization[65]. That is, a supercell with the same number of up and down moments is considered with a pair correlation function same as $A_{50}B_{50}$ random alloys, generated using the alloy theoretic automated toolkit code[66]. It is noted that our results reveal that systematic treatment of the PM state is needed in order to provide a quantitative description of the magnetostructural coupling in such compounds, where the recently developed spin-lattice dynamics approach is promising for future detailed investigations[67].

Anomalous Hall and Nernst conductivity calculation

The AHC is evaluated using the WannierTools code[68], where the required accurate tight-binding models are obtained by the maximally localized Wannier functions (MLWFs) using the Wannier90 code[69]. The s, p, and d orbitals of M and X atoms and the s and p orbitals for N atom are considered, resulting in 80 MLWFs in total for every noncollinear APVs. The AHC is computed by integrating the Berry curvature on a uniform $401 \times 401 \times 401$ k-points mesh to guarantee good accuracy, which can be expressed as[70]:

$$\sigma_{xy} = -\frac{e^2}{\hbar}\int \frac{d\mathbf{k}}{(2\pi)^3}\sum_n f[\epsilon(\mathbf{k}) - \mu]\Omega_{n,xy}(\mathbf{k}) \tag{3}$$

$$\Omega_{n,xy}(\mathbf{k}) = -2\mathrm{Im}\sum_{m\neq n}\frac{\langle\psi_{\mathbf{k}n}|v_x|\psi_{\mathbf{k}m}\rangle\langle\psi_{\mathbf{k}m}|v_y|\psi_{\mathbf{k}n}\rangle}{[\epsilon_m(\mathbf{k}) - \epsilon_n(\mathbf{k})]^2} \tag{4}$$

where e is elementary charge, μ is the chemical potential, $\psi_{n/m}$ denotes the Bloch wave function with energy eigenvalue $\epsilon_{n/m}$, $v_{x/y}$ is the velocity operator along Cartesian *x*/*y* direction, and $f[\epsilon(\mathbf{k}) - \mu]$ is Fermi-Dirac distribution function. The ANC α_{xy} is evaluated based on the Mott relation, which yields:

$$\alpha_{xy} = -\frac{\pi^2 k_B^2 T}{3e}\frac{d\sigma_{xy}}{d\epsilon}|_{\epsilon=\mu} \tag{5}$$

In this work, we evaluated only the derivative of AHC at the Fermi level $d\sigma_{xy}/d\epsilon$, which provides a quantitative measurements of the ANC.

DATA AVAILABILITY

All relevant computational results generated or analyzed during this study are included in the manuscript and Supplementary information files in the form of tables and figures.

CODE AVAILABILITY

The AHC was calculated using open source code Wannier90 and WannierTools. Postprocessing scripts used to calculate the derivative of AHC can be provided on request from the corresponding authors.

Received: 23 September 2020; Accepted: 3 June 2021;
Published online: 30 June 2021

REFERENCES

1. Fiebig, M., Lottermoser, T., Meier, D. & Trassin, M. The evolution of multiferroics. *Nat. Rev. Mater.* **1**, 16046–16059 (2016).
2. Trassin, M. Low energy consumption spintronics using multiferroic heterostructures. *J. Phys. Condens. Matter* **28**, 033001–033016 (2015).
3. Ma, J., Hu, J., Li, Z. & Nan, C.-W. Recent progress in multiferroic magnetoelectric composites: from bulk to thin films. *Adv. Mater.* **23**, 1062–1087 (2011).
4. Spaldin, N. A. & Fiebig, M. The renaissance of magnetoelectric multiferroics. *Science* **309**, 391–392 (2005).
5. Quintela, C. X. et al. Epitaxial antiperovskite/perovskite heterostructures for materials design. *Sci. Adv.* **6**, eaba4017–eaba4023 (2020).
6. Lukashev, P., Sabirianov, R. F. & Belashchenko, K. Theory of the piezomagnetic effect in mn-based antiperovskites. *Phys. Rev. B* **78**, 184414–184418 (2008).
7. Shao, D.-F., Gurung, G., Paudel, T. R. & Tsymbal, E. Y. Electrically reversible magnetization at the antiperovskite/perovskite interface. *Phys. Rev. Mater.* **3**, 024405–024413 (2019).
8. Zemen, J., Gercsi, Z. & Sandeman, K. G. Piezomagnetism as a counterpart of the magnetovolume effect in magnetically frustrated mn-based antiperovskite nitrides. *Phys. Rev. B* **96**, 024451–024458 (2017).
9. Boldrin, D. et al. Giant piezomagnetism in mn_3nin. *ACS Appl. Mater. Interfaces* **10**, 18863–18868 (2018).
10. Lin, J. et al. Giant negative thermal expansion covering room temperature in nanocrystalline gan_xmn_3. *Appl. Phys. Lett.* **107**, 131902–131906 (2015).
11. Takenaka, K. et al. Magnetovolume effects in manganese nitrides with antiperovskite structure. *Sci. Technol. Adv. Mater.* **15**, 015009–015019 (2014).
12. Takenaka, K. & Takagi, H. Giant negative thermal expansion in ge-doped antiperovskite manganese nitrides. *Appl. Phys. Lett.* **87**, 261902–261904 (2005).
13. Matsunami, D., Fujita, A., Takenaka, K. & Kano, M. Giant barocaloric effect enhanced by the frustration of the antiferromagnetic phase in mn_3gan. *Nat. Mater.* **14**, 73–78 (2015).
14. Peng, T., Bo-Sen, W. & Yu-Ping, S. Mn-based antiperovskite functional materials: review of research. *Chinese Phys. B* **22**, 067501–067512 (2013).
15. Shi, K. et al. Baromagnetic effect in antiperovskite $mn_3ga_{0.95}n_{0.94}$ by neutron powder diffraction analysis. *Adv. Mater.* **28**, 3761–3767 (2016).
16. Tohei, T., Wada, H. & Kanomata, T. Negative magnetocaloric effect at the antiferromagnetic to ferromagnetic transition of mn_3gac. *J. Appl. Phys.* **94**, 1800–1802 (2003).
17. Boldrin, D. et al. Multisite exchange-enhanced barocaloric response in mn_3nin. *Phys. Rev. X* **8**, 041035–041041 (2018).
18. Wang, B. et al. Large magnetic entropy change near room temperature in antiperovskite $sncmn_3$. *EPL* **85**, 47004–47008 (2009).
19. He, T. et al. Superconductivity in the non-oxide perovskite $mgcni_3$. *Nature* **411**, 54–56 (2001).
20. Lin, S. et al. Good thermoelectric performance in strongly correlated system $sncco_3$ with antiperovskite structure. *Inorg. Chem.* **53**, 3709–3715 (2014).
21. Shibayama, T. & Takenaka, K. Giant magnetostriction in antiperovskite mn_3cun. *J. Appl. Phys.* **109**, 07A928–07A930 (2011).
22. Chen, H., Niu, Q. & MacDonald, A. H. Anomalous Hall effect arising from noncollinear antiferromagnetism. *Phys. Rev. Lett.* **112**, 017205–017209 (2014).
23. Jungwirth, T., Marti, X., Wadley, P. & Wunderlich, J. Antiferromagnetic spintronics. *Nat. Nanotechnol.* **11**, 231–241 (2016).
24. Baltz, V. et al. Antiferromagnetic spintronics. *Rev. Mod. Phys.* **90**, 015005–015061 (2018).
25. Žutić, I., Fabian, J. & Das Sarma, S. Spintronics: fundamentals and applications. *Rev. Mod. Phys.* **76**, 323–410 (2004).
26. Liu, E. et al. Giant anomalous Hall effect in a ferromagnetic kagome-lattice semimetal. *Nat. Phys.* **14**, 1125–1131 (2018).

27. Xu, G., Lian, B. & Zhang, S.-C. Intrinsic quantum anomalous Hall effect in the kagome lattice $cs_2limn_3f_{12}$. *Phys. Rev. Lett.* **115**, 186802–186805 (2015).
28. Wang, Q., Sun, S., Zhang, X., Pang, F. & Lei, H. Anomalous Hall effect in a ferromagnetic fe_3sn_2 single crystal with a geometrically frustrated fe bilayer kagome lattice. *Phys. Rev. B* **94**, 075135–075139 (2016).
29. Gurung, G., Shao, D.-F., Paudel, T. R. & Tsymbal, E. Y. Anomalous Hall conductivity of noncollinear magnetic antiperovskites. *Phys. Rev. Mater.* **3**, 044409–044416 (2019).
30. Samathrakis, I. & Zhang, H. Tailoring the anomalous Hall effect in the noncollinear antiperovskite mn_3gan. *Phys. Rev. B* **101**, 214423–214428 (2020).
31. Boldrin, D. et al. Anomalous Hall effect in noncollinear antiferromagnetic mn_3nin thin films. *Phys. Rev. Mater.* **3**, 094409–094415 (2019).
32. Zhou, X. et al. Spin-order dependent anomalous Hall effect and magneto-optical effect in the noncollinear antiferromagnets mn_3xn with x = ga, zn, ag, or ni. *Phys. Rev. B* **99**, 104428–104440 (2019).
33. Gallego, S. V., Etxebarria, J., Elcoro, L., Tasci, E. S. & Perez-Mato, J. M. Automatic calculation of symmetry-adapted tensors in magnetic and non-magnetic materials: a new tool of the bilbao crystallographic server. *Acta Crystallogr A Found Adv.* **75**, 438–447 (2019).
34. Guo, G.-Y. & Wang, T.-C. Large anomalous nernst and spin nernst effects in the noncollinear antiferromagnets mn_3x (x = sn, ge, ga). *Phys. Rev. B* **96**, 224415–224423 (2017).
35. Kübler, J. & Felser, C. Non-collinear antiferromagnets and the anomalous Hall effect. *EPL* **108**, 67001–67005 (2014).
36. Nayak, A. K. et al. Large anomalous Hall effect driven by a nonvanishing berry curvature in the noncolinear antiferromagnet mn_3ge. *Sci. Adv.* **2**, e1501870–e1501874 (2016).
37. Bauer, G. E., Saitoh, E. & Van Wees, B. J. Spin caloritronics. *Nat. Mater.* **11**, 391–399 (2012).
38. Boona, S. R., Myers, R. C. & Heremans, J. P. Spin caloritronics. *Energy Environ. Sci.* **7**, 885–910 (2014).
39. Zhou, X. et al. Giant anomalous nernst effect in noncollinear antiferromagnetic mn-based antiperovskite nitrides. *Phys. Rev. Mater.* **4**, 024408–024415 (2020).
40. Sakai, A. et al. Giant anomalous nernst effect and quantum-critical scaling in a ferromagnetic semimetal. *Nat. Phys.* **14**, 1119–1124 (2018).
41. Guin, S. N. et al. Anomalous nernst effect beyond the magnetization scaling relation in the ferromagnetic heusler compound co_2mnga. *NPG Asia Mater.* **11**, 11–16 (2019).
42. Singh, H. K. et al. High-throughput screening of magnetic antiperovskites. *Chem. Mater.* **30**, 6983–6991 (2018).
43. Liu, Z. et al. Antiferromagnetic piezospintronics. *Adv. Electron. Mater.* **5**, 1900176–1900184 (2019).
44. Bouchaud, J.-P. et al. Antiferromagnetic-ferromagnetic transition in the compound mn3gac. *J. Appl. Phys.* **37**, 971–972 (1966).
45. Kenmotsu, A., Shinohara, T. & Watanabe, H. Nuclear magnetic resonance of ferromagnetic mn3alc and mn3gac. *J. Phys. Soc. Jpn.* **32**, 377–381 (1972).
46. Kanomata, T., Kaneko, T. & Nakagawa, Y. Magnetic properties of the intermetallic compound mn3inc. *J. Solid State Chem.* **96**, 451–454 (1992).
47. Fruchart, D. & F. Bertaut, E. Magnetic studies of the metallic perovskite-type compounds of manganese. *J. Phys. Soc. Jpn.* **44**, 781–791 (1978).
48. Fruchart, D., Bertaut, E., Senateur, J. & Fruchart, R. Magnetic studies on the metallic perovskite-type compound mn_3snn. *J. Phys. Lett.* **38**, 21–23 (1977).
49. Deng, S. et al. Frustrated triangular magnetic structures of mn_3znn: applications in thermal expansion. *J. Phys. Chem. C* **119**, 24983–24990 (2015).
50. Huyen, V. T. N., Suzuki, M.-T., Yamauchi, K. & Oguchi, T. Topology analysis for anomalous Hall effect in the noncollinear antiferromagnetic states of mn_3an (a = ni, cu, zn, ga, ge, pd, in, sn, ir, pt). *Phys. Rev. B* **100**, 094426–094434 (2019).
51. Giannozzi, P. et al. Quantum Espresso: a modular and open-source software project for quantum simulations of materials. *J. Phys. Condens. Matter.* **21**, 395502–395520 (2009).
52. Antropov, V., Ke, L. & Åberg, D. Constituents of magnetic anisotropy and a screening of spin–orbit coupling in solids. *Solid State Commun.* **194**, 35–38 (2014).
53. Buschow, K. H. J. *Handbook of Magnetic Materials*, Vol. 13 (Elsevier, 2003).
54. Abrikosov, I. A., Ponomareva, A., Steneteg, P., Barannikova, S. & Alling, B. Recent progress in simulations of the paramagnetic state of magnetic materials. *Curr. Opin. Solid State Mater. Sci.* **20**, 85–106 (2016).
55. Bocarsly, J. D. et al. A simple computational proxy for screening magnetocaloric compounds. *Chem. Mater.* **29**, 1613–1622 (2017).
56. Date, M., Kanamori, J. & Tachiki, M. Origin of magnetoelectric effect in cr_2o_3. *J. Phys. Soc. Jpn.* **16**, 2589–2589 (1961).
57. Ryu, J., Priya, S., Uchino, K. & Kim, H.-E. Magnetoelectric effect in composites of magnetostrictive and piezoelectric materials. *J. Eelectroceram.* **8**, 107–119 (2002).
58. Tashiro, H., Suzuki, R., Miyawaki, T., Ueda, K. & Asano, H. Preparation and properties of inverse perovskite mn_3gan thin films and heterostructures. *J. Korean Phys. Soc.* **63**, 299–301 (2013).
59. Nagaosa, N., Sinova, J., Onoda, S., MacDonald, A. H. & Ong, N. P. Anomalous Hall effect. *Rev. Mod. Phys.* **82**, 1539–1592 (2010).
60. Xiao, D., Yao, Y., Fang, Z. & Niu, Q. Berry-phase effect in anomalous thermoelectric transport. *Phys. Rev. Lett.* **97**, 026603–026606 (2006).
61. Noky, J., Gooth, J., Felser, C. & Sun, Y. Characterization of topological band structures away from the fermi level by the anomalous nernst effect. *Phys. Rev. B* **98**, 241106–241110 (2018).
62. Sakai, A. et al. Iron-based binary ferromagnets for transverse thermoelectric conversion. *Nature* **581**, 53–57 (2020).
63. Kresse, G. & Furthmüller, J. Efficient iterative schemes for ab initio total-energy calculations using a plane-wave basis set. *Phys. Rev. B* **54**, 11169–11186 (1996).
64. Perdew, J. P., Burke, K. & Ernzerhof, M. Generalized gradient approximation made simple. *Phys. Rev. Lett.* **77**, 3865–3868 (1996).
65. Zunger, A., Wei, S.-H., Ferreira, L. G. & Bernard, J. E. Special quasirandom structures. *Phys. Rev. Lett.* **65**, 353–356 (1990).
66. van de Walle, A., Asta, M. D. & Ceder, G. The Alloy Theoretic Automated Toolkit: a user guide. *Calphad* **26**, 539–553 (2002).
67. Stockem, I. et al. Anomalous phonon lifetime shortening in paramagnetic crn caused by spin-lattice coupling: a combined spin and ab initio molecular dynamics study. *Phys. Rev. Lett.* **121**, 125902–125907 (2018).
68. Wu, Q., Zhang, S., Song, H.-F., Troyer, M. & Soluyanov, A. A. Wanniertools: an open-source software package for novel topological materials. *Comput. Phys. Commun.* **224**, 405–416 (2018).
69. Mostofi, A. A. et al. wannier90: a tool for obtaining maximally-localised wannier functions. *Comput. Phys. Commun.* **178**, 685–699 (2008).
70. Xiao, D., Chang, M.-C. & Niu, Q. Berry phase effects on electronic properties. *Rev. Mod. Phys.* **82**, 1959–2007 (2010).
71. Bertaut, E., Fruchart, D., Bouchaud, J. & Fruchart, R. Diffraction neutronique de mn_3gan. *Solid State Commun.* **6**, 251–256 (1968).

ACKNOWLEDGEMENTS

The authors are grateful and acknowledge TU Darmstadt Lichtenberg high-performance computer support for the computational resources where the calculations were conducted for this project. The authors thank Prof. Manuel Richter of IFW Dresden for providing the SOC strength data and discussion. This project was supported by the Deutsche Forschungsgemeinschaft (DFG, German Research Foundation) Project-ID 405553726-TRR 270. N.M.F. acknowledges European Research Council (ERC) funding for financial support under the European Union's Horizon 2020 research and innovation programme (Grant No. 743116 project Cool Innov). The work of J.Z. was supported by the Ministry of Education, Youth and Sports of the Czech Republic from the OP RDE program under the project International Mobility of Researchers MSCA-IF at CTU No. CZ.02.2.69/0.0/0.0/18_070/0010-457.

AUTHOR CONTRIBUTIONS

H.K.S. preformed all the calculations. All authors discussed the results. The manuscript was written by H.K.S. All authors reviewed and approved the manuscript.

FUNDING

Open Access funding enabled and organized by Projekt DEAL.

COMPETING INTERESTS

The authors declare no competing interests.

ADDITIONAL INFORMATION

Supplementary information The online version contains supplementary material available at https://doi.org/10.1038/s41524-021-00566-w.

Correspondence and requests for materials should be addressed to H.K.S. or H.Z.

Reprints and permission information is available at http://www.nature.com/reprints

Publisher's note Springer Nature remains neutral with regard to jurisdictional claims in published maps and institutional affiliations.